

Superconductivity in Hexagonal Zr_6CoAl_2 -Type Zr_6RuBi_2 and Zr_6FeBi_2

Kosuke Yuchi*, Daisuke Nishio-Hamane, Keita Kojima, Kodai Moriyama,
Ryutaro Okuma, and Yoshihiko Okamoto†

Institute for Solid State Physics, University of Tokyo, Kashiwa 277-8581, Japan

We report the synthesis and electronic properties of polycrystalline samples of Zr_6MBi_2 ($M = Ru$ and Fe) crystallizing in the hexagonal Zr_6CoAl_2 -type structure. Based on their electrical resistivity, magnetization, and heat capacity data, Zr_6RuBi_2 and Zr_6FeBi_2 are found to exhibit bulk superconductivity below $T_c = 4.9$ and 1.4 K, respectively. Although Zr_6RuBi_2 is most likely a conventional superconductor, the considerably higher T_c for $M = Ru$ than that for $M = Fe$ differs from the trend in T_c for Zr_6CoAl_2 -type superconductors reported thus far. The superconductivity of an amorphous solid-solution phase, which may hinder elucidation of the superconducting properties of Zr_6MBi_2 , is also discussed.

Recently, new superconductors have been discovered in A_6MX_2 compounds with the hexagonal Zr_6CoAl_2 -type crystal structure. Figure 1(a) shows this crystal structure, which is an ordered Fe_2P type with the noncentrosymmetric space group $P-62m$. The discovery of superconductors in the A_6MX_2 family was triggered by Sc_6MTe_2 , which was found to exhibit superconductivity in the cases of seven transition metals M ($M = Fe, Co, Ni, Ru, Rh, Os, \text{ and } Ir$) [1]. The superconducting transition temperature T_c is approximately 2 K for $M = 4d$ and $5d$ transition metals, whereas in the $M = 3d$ cases, T_c increases in the order of $Ni, Co, \text{ and } Fe$ with the highest value of $T_c = 4.7$ K being observed for Sc_6FeTe_2 . Subsequently, Zr_6FeTe_2 , Zr_6CoTe_2 , and Zr_6FeSb_2 were found to exhibit superconductivity at lower temperatures than Sc_6MTe_2 [2,3]. According to the results of first-principles calculations, electronic states near the Fermi level in Sc_6MTe_2 and Zr_6MTe_2 mainly consist of d orbitals of M and Sc/Zr atoms, and especially in Sc_6FeTe_2 , which shows the highest T_c , the contribution of the $Fe 3d$ orbitals is considerably large [1,2,4]. Sc_6FeTe_2 has also been shown to have a strong lattice anharmonicity compared to other Sc_6MTe_2 due to the rattling of Fe atoms [4], which may be related to the high T_c of this material. In contrast, Sc_6MnTe_2 and Zr_6MnTe_2 do not exhibit superconductivity, but show strong magnetism originating from the $Mn 3d$ electrons [1,2]. Thus, Zr_6CoAl_2 -type A_6MX_2 constitute a d -electron superconductor family, in which the d electrons of the M and A atoms are strongly involved in the emergence of superconductivity, making them a potential target for studying the correlation between superconductivity and various features of transition metals.

As a superconductor family, a remarkable feature of A_6MX_2 is that the $A, M, \text{ and } X$ atoms can all be changed to various elements. For example, both Sc_6NiTe_2 and Zr_6FeSb_2 exhibit superconductivity. In Zr_6CoAl_2 -type A_6MX_2 , the A atoms can be $Sc, Y, Zr, Hf, \text{ or the heavy lanthanides, the } M$

atoms can be almost all transition metals, and the X atoms can be various electronegative elements of groups 13 to 16. The number of the permutations of these $A, M, \text{ and } X$ atoms is very large, and over 100 materials have been synthesized to date [1-3, 5-25]. There have been many studies on the physical properties of A_6MX_2 compounds, including on the spin structure of the magnetically ordered phase [22, 25-29] and their magnetocaloric properties [30-32]. However, to the best of our knowledge, there are no reports on superconductivity other than on the above ten materials [1-3] and many A_6MX_2 compounds have yet to be characterized, raising expectation that many d -electron superconductors will be discovered in this family.

In this letter, we focus on Zr_6MBi_2 ($M = Ru$ and Fe) crystallizing in the Zr_6CoAl_2 -type structure. For $M = Mn, Fe, Co, Ni, Cu, \text{ and } Rh$, polycrystalline samples have been synthesized, and the crystal structure was reported to be of the Zr_6CoAl_2 type [11, 20, 25]. Polycrystalline samples of Zr_6FeBi_2 and Zr_6CoBi_2 were found to show metallic electrical resistivity above 4.2 K [11]. No superconductivity has been reported, even when extending the range to all A_6MX_2 members with $X = Bi$. New superconductors with $X = Bi$ will provide an insight into heavy element effects of the X atoms on superconductivity. In the case of Sc_6MTe_2 , $M = Os$ and Ir exhibit lower T_c values than those of $M = Fe$ and Co , but considerably higher upper critical fields H_{c2} for their T_c values, suggesting that strong spin-orbit coupling of the $5d$ electrons of M atoms plays a role [1].

Polycrystalline samples of Zr_6MBi_2 ($M = Ru$ and Fe) were synthesized by the arc-melting of Zr chips (99.9%, RARE METALLIC), Ru (99.95%, RARE METALLIC) or Fe (99.5%, RARE METALLIC) powder, and Bi chips (99.99%, Wako Pure Chemical Corp.). First, 6:1.5:2.5 and 6:1:2.5 molar ratios of Zr chips, M powder, and Bi chips for $M = Ru$ and Fe were respectively placed on a water-cooled copper hearth and arc-

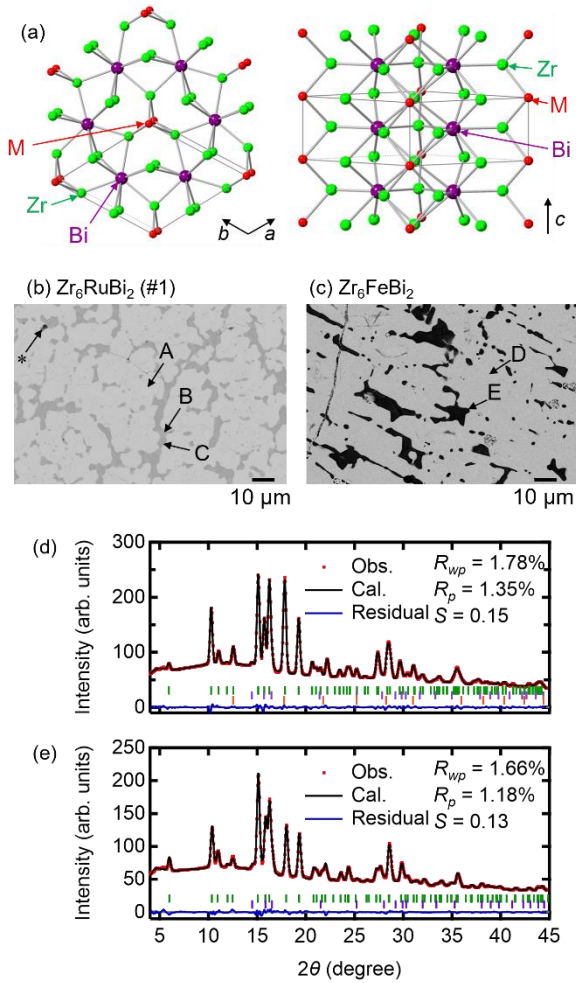


Figure 1. (a) Crystal structure of Zr_6MBi_2 ($M = Ru$ and Fe) viewed along (left) and perpendicular to (right) the c axis. The solid lines indicate the unit cell. (b, c) SEM images of (b) Zr_6RuBi_2 (sample #1) and (c) Zr_6FeBi_2 polycrystalline samples. In (b), the black area marked with an asterisk is a void. (d, e) Powder XRD patterns of (d) Zr_6RuBi_2 (sample #1) and (e) Zr_6FeBi_2 polycrystalline samples acquired at room temperature using R-AIXS RAPID-II ($Mo\ K\alpha$). Filled circles show experimental data. The overlapped curve shows the calculated pattern, whereas the lower curve shows a difference plot between the experimental and calculated intensities. The top (green), second (purple), and third (orange, Zr_6RuBi_2 only) vertical bars indicate the position of the Bragg reflections of the Zr_6MBi_2 , Zr, and ZrRu phases, respectively. The S values are small caused by high background intensity due to X-ray fluorescence.

melted under an Ar atmosphere. The obtained buttons were subsequently inverted and arc-melted several times to promote homogenization. They were then annealed in evacuated quartz tubes at 1273 K for 216 h. For Zr_6RuBi_2 , the sample prepared by this procedure is named as sample #1. Hereinafter, mainly the experimental data for this sample are presented, and those of the sample #2, prepared under different conditions are only presented in the last part of this letter. Unless specified otherwise, we refer to sample #1. For Zr_6FeBi_2 , all of the experimental data presented herein were

obtained using this sample. Microstructural observations and chemical analyses were conducted by means of a scanning electron microscope (SEM; JEOL IT-100) equipped with an attachment for energy-dispersive X-ray spectroscopy (EDX; 15 kV, 0.8 nA, 1 μm beam diameter). The ZAF method was used for data correction, and the standards used were samples of the pure metals. Powder X-ray diffraction (XRD) measurements on Zr_6RuBi_2 (sample #1) and Zr_6FeBi_2 were performed on a Debye-Scherrer diffractometer R-AXIS RAPID II (RIGAKU) using $Mo\ K\alpha$ radiation at room temperature. Details on the measurements are described in Supplementary Note 2. The structural analysis was performed using JANA2006 [33]. A powder XRD measurement on Zr_6RuBi_2 (sample #2) was performed on a Bragg-Brentano diffractometer MiniFlex600-C (RIGAKU) using $Cu\ K\alpha$ radiation at room temperature. Electrical resistivity and heat capacity measurements were performed using a Physical Property Measurement System (Quantum Design). Magnetization measurements were performed using an MPMS-3 (Quantum Design). Electrical resistivity measurements down to 0.1 K were performed using an adiabatic demagnetization refrigerator. Heat capacity and magnetization measurements down to 0.5 K were performed using a 3He refrigerator.

Figures 1(b) and 1(c) show SEM images of polycrystalline samples of Zr_6RuBi_2 (sample #1) and Zr_6FeBi_2 , respectively. In the SEM image of Zr_6RuBi_2 , the white area marked A is the main phase, which is accompanied by two minor phases marked B and C (B and C areas are both gray, but area B is slightly paler than area C. Figures that allow the difference between B and C areas to be more easily recognized are shown in Supplementary Fig. 1). The percentages of phases A, B, and C of the total area are 81%, 9%, and 9%, respectively. The chemical compositions of phases A, B, and C were determined by EDX as $Zr_{6.06(2)}Ru_{1.00(1)}Bi_{1.94(1)}$, $Zr_{0.51}Ru_{0.49}$, and $Zr_{0.99}Bi_{0.01}$, respectively, where the total number of atoms is fixed to be nine for phase A and one for phases B and C. The results indicate that all three phases are almost stoichiometric. Considering the small degree of nonstoichiometry and powder XRD results described below, the chemical formulae of phases A, B, and C are expressed as Zr_6RuBi_2 , ZrRu, and Zr, respectively. Among these phases, ZrRu and Zr do not show superconductivity. In the SEM image of Zr_6FeBi_2 shown in Fig. 1(c), the gray region marked D is the main phase and the black region marked E is a minor phase. The percentages of the phases D and E of the total area are 89% and 11%, respectively. The EDX chemical analysis as applied to Zr_6RuBi_2 showed the chemical compositions of phases D and E to be $Zr_{6.07(1)}Fe_{0.98(2)}Bi_{1.95(1)}$ and $Zr_{0.987}Fe_{0.007}Bi_{0.006}$, respectively. As in the case of Zr_6RuBi_2 , considering the small degree of nonstoichiometry and powder XRD results, the chemical formulae of these phases are expressed as Zr_6FeBi_2 and Zr, respectively. The Zr phase does not exhibit super-

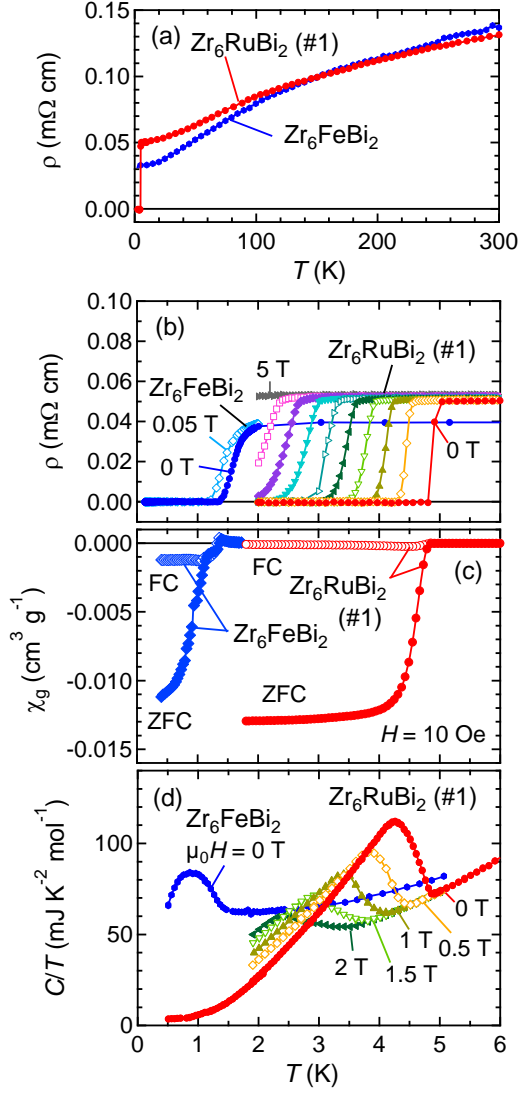


Figure 2. Electronic properties of polycrystalline samples of Zr_6RuBi_2 (sample #1) and Zr_6FeBi_2 . (a) Temperature dependence of electrical resistivity of Zr_6RuBi_2 and Zr_6FeBi_2 measured above 2 K. (b) Temperature dependence of electrical resistivity of Zr_6RuBi_2 at $\mu_0H = 0, 0.5, 1, 1.5, 2, 2.5, 3, 3.5, 4,$ and 5 T and of Zr_6FeBi_2 at $\mu_0H = 0$ and 0.05 T. (c) Temperature dependence of FC and ZFC magnetic susceptibility of Zr_6RuBi_2 and Zr_6FeBi_2 measured at a magnetic field of 10 Oe. (d) Temperature dependence of heat capacity divided by temperature for Zr_6RuBi_2 measured at various magnetic fields and Zr_6FeBi_2 at zero magnetic field. The C/T data were calculated assuming each sample to consist of a single phase of Zr_6MBi_2 .

conductivity. These SEM and EDX results clearly show that each sample contains Zr_6MBi_2 as the main phase, accompanied by nonsuperconducting minor phases.

Figures 1(d) and 1(e) shows the powder XRD patterns of Zr_6RuBi_2 (sample #1) and Zr_6FeBi_2 polycrystalline samples, respectively, along with the results of their Rietveld analyses. The crystallographic parameters determined from these analyses are listed in Supplementary Table I. Consistent with the SEM and EDX results, diffraction peaks of Zr are present

in the XRD patterns of both samples and those of $ZrRu$ are present in that of Zr_6RuBi_2 . Therefore, we performed multiphase analyses including these impurity phases. In each case, the difference between experimental and calculated intensities was minimized when a hexagonal Zr_6CoAl_2 -type structural model was used for the main phase, indicating that Zr_6CoAl_2 -type Zr_6MBi_2 was obtained as the main phase for both $M = Ru$ and Fe . The lattice parameters were refined to $a = 7.9181(3)$ Å and $c = 3.6847(2)$ Å for $M = Ru$ and $a = 7.8629(4)$ Å and $c = 3.7174(3)$ Å for $M = Fe$. To the best of our knowledge, Zr_6RuBi_2 has not been reported previously. However, the a and c values of Zr_6FeBi_2 are consistent with those of a previous study [11].

Figures 2(a) and 2(b) show the temperature dependences of electrical resistivity, ρ , of the Zr_6RuBi_2 (sample #1) and Zr_6FeBi_2 polycrystalline samples. As shown in Fig. 2(a), both samples showed metallic ρ , which decreased with decreasing temperature. The residual resistivity ratios, $RRR = \rho_{300K}/\rho_0$, where ρ_{300K} is ρ at 300 K and ρ_0 is the residual resistivity, were evaluated as 2.6 and 4.5 for Zr_6RuBi_2 and Zr_6FeBi_2 , respectively. At lower temperatures, the ρ of both samples showed a sharp drop to zero. The onset and zero-resistivity temperatures were determined as 5.0 and 4.8 K for Zr_6RuBi_2 and 2.0 and 1.4 K for Zr_6FeBi_2 , respectively.

As shown in Fig. 2(c), the zero-field-cooled (ZFC) and field-cooled (FC) magnetization data of Zr_6RuBi_2 (sample #1) and Zr_6FeBi_2 polycrystalline samples showed strong diamagnetic signals due to superconductivity below 4.9 and 1.4 K, respectively. The shielding fractions of Zr_6RuBi_2 (1.8 K) and Zr_6FeBi_2 (0.4 K), evaluated by assuming a single phase of Zr_6MBi_2 , were determined as 144% and 120%, respectively. Furthermore, as shown in Fig. 2(d), the values of heat capacity divided by temperature, C/T , of the polycrystalline samples of Zr_6RuBi_2 (sample #1) and Zr_6FeBi_2 strongly increased from 4.9 and 1.4 K and reached maxima at 4.2 and 0.9 K, respectively, with decreasing temperature. These results clearly indicate that both samples exhibited bulk superconductivity. Considering the midpoint of the resistivity drop, the onset of the magnetization drop, and the onset of the heat capacity jump, T_c was determined as 4.9 and 1.4 K for $M = Ru$ and Fe , respectively.

In the following, we discuss superconducting properties on the basis of heat capacity data. As shown in Fig. 3(a), normal-state C/T for both $M = Ru$ and Fe are linear with respect to T^2 at low temperatures. The solid lines show the results of fitting to the equation $C/T = AT^2 + \gamma$, where A and γ represent the coefficient of the T^3 term of the lattice heat capacity and Sommerfeld coefficient, respectively. The T^3 term and Sommerfeld coefficient for Zr_6RuBi_2 and Zr_6FeBi_2 were estimated as $A = 1.563(9)$ and $0.72(1)$ $mJ K^{-4} mol^{-1}$ and $\gamma = 34.7(1)$ and $59.37(9)$ $mJ K^{-2} mol^{-1}$, respectively. Temperature dependence of the electronic heat capacity divided by temperature, C_{el}/T , obtained by subtracting the lattice contribution from experimental data, i.e., $C_{el}/T = C/T - AT^2$,

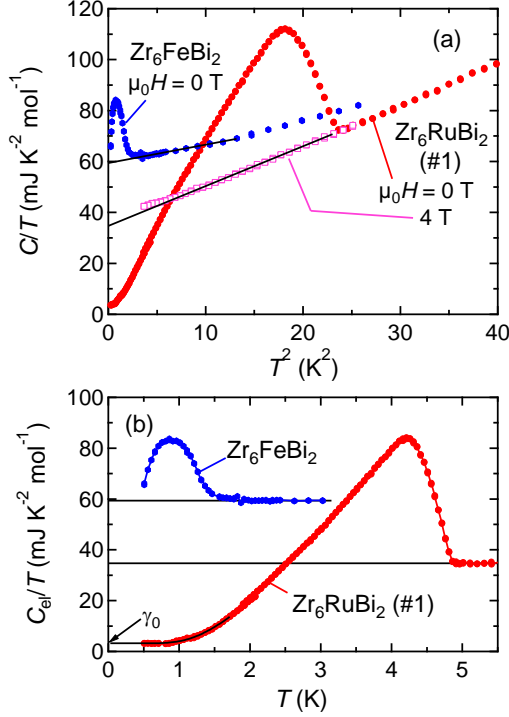


Figure 3. (a) Heat capacity divided by temperature of Zr_6RuBi_2 (sample #1) and Zr_6FeBi_2 polycrystalline samples as a function of T^2 , calculated assuming a single phase of Zr_6MBi_2 . The solid lines show the results of linear fits of the 4 T data for Zr_6RuBi_2 between 3 and 4.8 K and zero-field data for Zr_6FeBi_2 between 2 and 3.6 K. (b) Temperature dependence of electronic heat capacity divided by temperature for Zr_6RuBi_2 and Zr_6FeBi_2 obtained by subtracting the lattice contribution from the C/T data. The solid lines indicate the normal state γ for each compound. The solid curve on the Zr_6RuBi_2 data shows a fitting to the equation $C_{el} = \gamma_0 T + B \exp[-\Delta(0)/k_B T]$.

is plotted in Fig. 3(b). The C_{el}/T data of Zr_6RuBi_2 below $0.35T_c$ were fitted to the equation $C_{el} = \gamma_0 T + B \exp[-\Delta(0)/k_B T]$, where $\Delta(0)$ is the size of the superconducting gap at zero temperature. The result of this fitting is reasonably good, suggesting the presence of an isotropic gap and yielding $\gamma_0 = 3.20(6)$ mJ K⁻² mol⁻¹, $B = 1.3(1) \times 10^3$ mJ K⁻¹ mol⁻¹, and $\Delta(0)/k_B = 7.4(1)$ K. The obtained γ_0 is 9% of γ , suggesting that the majority of the sample is superconducting at the lowest temperature.

Using the heat capacity jump at T_c of $\Delta C_{el}/T_c = 49.5$ mJ K⁻² mol⁻¹ and the superconducting contribution of the Sommerfeld coefficient $\gamma_s = \gamma - \gamma_0 = 31.5$ mJ K⁻² mol⁻¹, the magnitude of the jump in Zr_6RuTe_2 was estimated as $\Delta C_{el}/\gamma_s T_c = 1.6$. This value is somewhat underestimated by a gradual change of C_{el}/T at T_c , suggesting that the actual $\Delta C_{el}/\gamma_s T_c$ is slightly larger than the weak-coupling limit value of 1.43 for a conventional Bardeen–Cooper–Schrieffer (BCS) superconductor. This result suggests that the superconductivity in Zr_6RuBi_2 is most likely a strong-coupling BCS superconductivity, which would be consistent with the observation that the low-temperature C_{el} is well-fitted by the exponential

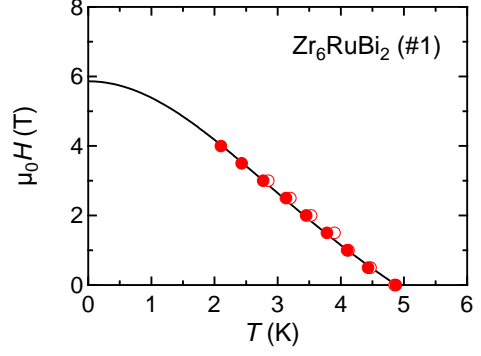


Figure 4. Magnetic field versus midpoint temperatures in the resistivity drop (filled circles) and onset temperatures in the heat capacity jump (open circles) for polycrystalline Zr_6RuBi_2 (sample #1). The solid curve shows a fitting to the Ginzburg–Landau formula.

function, as shown in Fig. 3(b). In contrast, γ_0 of Zr_6FeBi_2 could not be determined due to the low T_c . Moreover, the broad jump in C_{el}/T , as shown in Fig. 3(b), does not allow an accurate estimate of ΔC_{el} . In order to discuss the superconducting properties of Zr_6FeBi_2 based on the heat capacity data, it would be necessary to perform experiments at lower temperatures using a sample of higher quality.

The superconducting properties of Zr_6RuBi_2 under magnetic fields can be discussed on the basis of the ρ and C/T data measured in various magnetic fields, as shown in Figs. 2(b) and 2(d), respectively. As shown in Fig. 4, the midpoint of the decrease in ρ , T_c^{mid} , and the onset of T_c of heat capacity jump show similar trends in magnetic fields, indicating that T_c^{mid} reflects the bulk superconducting transition. Fitting $H_{c2}(T)$ estimated from T_c^{mid} with the Ginzburg–Landau (GL) formula, $H_{c2}(T) = H_{c2}(0)[1 - (T/T_c^{\text{mid}})^2]/[1 + (T/T_c^{\text{mid}})^2]$, yields $\mu_0 H_{c2}(0) = 5.86(5)$ T and GL coherence length of $\xi = 0.75$ nm. This $H_{c2}(0)$ is considerably lower than the Pauli-limiting field of $\mu_0 H_{c2}(0)/T = 1.84T_c^{\text{mid}}/K = 9$ T [34], suggesting that the strong spin-orbit coupling of heavy elements does not significantly affect the superconducting properties of Zr_6RuBi_2 under magnetic fields, even though it has a noncentrosymmetric crystal structure and comprises heavy elements.

As discussed above, superconductivity in Zr_6RuBi_2 is most likely conventional, but it is noteworthy that its T_c is considerably higher than that of Zr_6FeBi_2 . We synthesized Zr_6MBi_2 samples with other M atoms such as Rh, Ir, and Co. However, no material other than M = Ru was confirmed to exhibit bulk superconductivity above 2 K, meaning that an anomalously high T_c is manifested in Zr_6RuBi_2 . This trend in T_c differs from that for Sc_6MTe_2 , where Sc_6FeTe_2 showed the highest T_c of 4.7 K [1]. Zr_6FeTe_2 also showed the highest T_c among Zr_6MTe_2 , although its T_c was much lower [2]. The fact that Zr_6RuBi_2 showed the highest T_c among the current A_6MX_2 members indicates that M being a 3d transition metal

element is not always advantageous for superconductivity, and that the combination of A, M, and X elements is important. In particular, $\gamma = 36.3 \text{ mJ K}^{-2} \text{ mol}^{-1}$ for Zr_6RuBi_2 is considerably smaller than $\gamma = 73 \text{ mJ K}^{-2} \text{ mol}^{-1}$ for Sc_6FeTe_2 ($T_c = 4.7 \text{ K}$) and $\gamma = 50 \text{ mJ K}^{-2} \text{ mol}^{-1}$ for Zr_6FeBi_2 ($T_c = 1.4 \text{ K}$), but is comparable to $\gamma = 40 \text{ mJ K}^{-2} \text{ mol}^{-1}$ for Sc_6RuTe_2 ($T_c = 1.9 \text{ K}$) [1]. It is surprising that the highest T_c in the A_6MX_2 family is achieved in Zr_6RuBi_2 . Future detailed elaboration of the trend in T_c in Zr_6MBi_2 based on the experimental results of other M cases and electronic structure calculation results will allow us to pursue the realization of a higher T_c in A_6MX_2 .

Finally, we discuss a difficulty regarding the study of superconductivity in Zr_6MBi_2 from a chemical point of view. Supplementary Fig. 2(a) shows a SEM image of a Zr_6RuBi_2 sample prepared by arc-melting of stoichiometric amounts of Zr, Ru, and Bi without annealing. This sample is hereinafter referred to as sample #2. As shown in this figure, sample #2 consisted of two different phases marked F (light-gray) and G (dark-gray). According to EDX analysis, phase F is the Zr_6RuBi_2 phase with the chemical composition $\text{Zr}_{6.03(4)}\text{Ru}_{0.82(3)}\text{Bi}_{2.15(3)}$, whereas phase G is a Zr-Ru-Bi solid solution with composition $\text{Zr}_{0.90}\text{Ru}_{0.05}\text{Bi}_{0.05}$. These Zr_6RuBi_2 and Zr-Ru-Bi solid-solution phases account for 61% and 39% of the total area, respectively, indicating that while Zr_6RuBi_2 is the main phase, the Zr-Ru-Bi solid solution is also present in a significant proportion. However, as shown in Supplementary Fig. 2(b), only the diffraction peaks of Zr_6RuBi_2 with the Zr_6RuBi_2 -type crystal structure appear in the powder XRD pattern of sample #2, indicating that the Zr-Ru-Bi solid-solution phase was amorphous. This amorphous phase could not be completely eliminated by annealing sample #2.

In sample #2, not only the Zr_6RuBi_2 phase but also the Zr-Ru-Bi solid solution exhibit superconductivity at a similar T_c . As shown by the C/T data in Supplementary Fig. 3(a), in addition to the peak at $T_{c1} = 4.3 \text{ K}$, there is a shoulder-like feature at around $T_{c2} = 4.6 \text{ K}$. As shown in Supplementary Fig. 3(b), the T_{c1} of sample #2 shows a similar variation under magnetic fields as that of sample #1, whereas the change in T_{c2} by applying a magnetic field is smaller than that of T_{c1} , suggesting that T_{c1} and T_{c2} correspond to the superconducting transitions of the Zr_6RuBi_2 and amorphous Zr-Ru-Bi phases, respectively. Amorphous phases comprising Zr and several percent of a transition metal element have been reported to exhibit superconductivity at $T_c = 4\text{--}6 \text{ K}$ [35], supporting the above consequence. The superconducting transition at T_{c2} appeared in Zr_6RuBi_2 samples synthesized under various conditions except for sample #1. In sample #1 of Zr_6RuBi_2 , the nominal chemical composition was shifted from the stoichiometric ratio and the sample was annealed under the appropriate conditions, resulting in suppression of formation of the amorphous superconducting phase. This amorphous superconducting phase hinders the exploration of new Zr_6MBi_2 superconductors. It is expected that new super-

conductors will be discovered in the A_6MX_2 family in future studies, but our results for sample #2 suggest that in this quest the possible formation of an amorphous impurity phase should always be borne in mind.

In summary, Zr_6CoAl_2 -type Zr_6RuBi_2 and Zr_6FeBi_2 have been identified as bulk superconductors with $T_c = 4.9 \text{ K}$ and 1.4 K , respectively, based on electrical resistivity, magnetization, and heat capacity measurements on polycrystalline samples. The T_c of Zr_6RuBi_2 is highest in the A_6MX_2 family. The superconductivity of Zr_6RuBi_2 is most likely a conventional BCS superconductivity both in a zero magnetic field and under magnetic fields. However, the considerably higher T_c for Zr_6RuBi_2 than that for Zr_6FeBi_2 differs from the trend for known A_6MX_2 superconductors. We hope that the exploration of new superconductors in the A_6MX_2 family will lead to the discovery of new superconductors with higher T_c or unusual properties. However, the possible formation of an amorphous superconducting phase should always be borne in mind, since this would hinder elucidation of the superconducting properties of A_6MX_2 .

Acknowledgments

The authors are grateful to H. Matsumoto, J. Yamaura, Z. Hiroi, and Y. Shinoda for helpful discussions. This work was supported by JSPS KAKENHI (Grant Nos. 23H01831 and 23K26524) and JST ASPIRE (Grant Number: JPMJAP2314).

References

- [1] Y. Shinoda, Y. Okamoto, Y. Yamakawa, H. Matsumoto, D. Hirai, and K. Takenaka, *J. Phys. Soc. Jpn.* **92**, 103701 (2023).
- [2] H. Matsumoto, Y. Yamakawa, R. Okuma, D. Nishio-Hamane, and Y. Okamoto, *J. Phys. Soc. Jpn.* **93**, 023705 (2024).
- [3] R. Matsumoto, E. Murakami, R. Oishi, S. Ramakrishnan, A. Ikeda, S. Yonezawa, T. Takabatake, T. Onimaru, and M. Nohara, *J. Phys. Soc. Jpn.* **93**, 065001 (2024).
- [4] M.-C. Jiang, R. Masuki, G.-Y. Guo, and R. Arita, arXiv:2405.10524.
- [5] Y.-U. Kwon, S. C. Sevov, and J. D. Corbett, *Chem. Mater.* **2**, 550 (1990).
- [6] F. Gingle, K. Yvon, I. Y. Zvaliy, V. A. Yartys', and P. Fischer, *J. Alloys Comp.* **226**, 1 (1995).
- [7] C. Wang and T. Hughbanks, *Inorg. Chem.* **35**, 6987 (1996).
- [8] H. Kleinke, *J. Alloys Comp.* **252**, L29 (1997).
- [9] H. Kleinke, *J. Alloys Comp.* **270**, 136 (1998).
- [10] I. Y. Zvaliy, V. K. Pecharsky, G. J. Miller, L. G. Akselrud, *J. Alloys Comp.* **283**, 106 (1999).
- [11] G. Melnyk, E. Bauer, P. Rogl, R. Skolozdra, E. Seidl, *J. Alloys Comp.* **296**, 235 (2000).
- [12] P. A. Maggard and J. D. Corbett, *Inorg. Chem.* **39**, 4143 (2000).
- [13] N. Bestaoui, P. S. Herle, and J. D. Corbett, *J. Solid State Chem.* **155**, 9 (2000).
- [14] F. Meng, C. Magliocchi, and T. Hughbanks, *J. Alloys Comp.* **358**, 98 (2003).

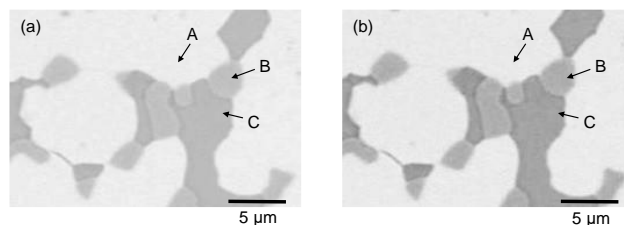
- [15] A. V. Morozkin, *J. Alloys Comp.* **353**, L16 (2003).
- [16] A. V. Morozkin, *J. Alloys Comp.* **358**, L9 (2003).
- [17] A. V. Morozkin, *J. Alloys Comp.* **360**, L1 (2003).
- [18] A. V. Morozkin, *J. Alloys Comp.* **360**, L7 (2003).
- [19] L. Chen and J. D. Corbett, *Inorg. Chem.* **43**, 436 (2004).
- [20] A. G. Bolotaev, A. L. Koroliuk, A. V. Morozkin, and V. N. Nikiforov, *J. Alloys Comp.* **373**, L1 (2004).
- [21] A. V. Morozkin, V. N. Nikiforov, and B. Malaman, *J. Alloys Comp.* **393**, L9 (2005).
- [22] A. V. Morozkin, R. Nirmala, and S. K. Malik, *J. Alloys Comp.* **394**, 75 (2005).
- [23] G. Cai, J. Zhang, W. He, P. Qin, and L. Zeng, *J. Alloys Comp.* **421**, 42 (2006).
- [24] A. V. Morozkin, Y. Mozharivskyj, V. Svitlyk, R. Nirmala, O. Isnard, P. Manfrinetti, A. Provino, C. Ritter, *J. Solid State Chem.* **183**, 1314 (2010).
- [25] A. V. Morozkin, R. Nirmala, and S. K. Malik, *Intermetallics* **19**, 1250 (2011).
- [26] A. V. Morozkin, V. N. Nikiforov, and B. Malaman, *J. Alloys Comp.* **393**, L6 (2005).
- [27] A. V. Morozkin, O. Isnard, P. Henry, P. Manfrinetti, R. Nirmala, and S. K. Malik, *J. Alloys Comp.* **450**, 62 (2008).
- [28] A. V. Morozkin, O. Isnard, P. Manfrinetti, A. Provino, C. Ritter, R. Nirmala, and S. K. Malik, *J. Alloys Comp.* **498**, 13 (2010).
- [29] A. V. Morozkin, Y. Mozharivskyj, V. Svitlyk, R. Nirmala, and A. K. Nigam, *J. Solid State Chem.* **183**, 3039 (2010).
- [30] A. Herrero, A. Oleaga, A. Salazar, A. V. Garshev, V. O. Yapaskurt, A. V. Morozkin, *J. Alloys Comp.* **821**, 153198 (2020).
- [31] A. Oleaga, A. Herrero, A. Salazar, A. V. Garshev, V. O. Yapaskurt, and A. V. Morozkin, *J. Alloys Comp.* **843**, 155937 (2020).
- [32] A. Herrero, A. Oleaga, I. R. Aseguinolaza, A. J. Garcia-Adeva, E. Apiñaniz, A. V. Garshev, V. O. Yapaskurt, A. V. Morozkin, *J. Alloys Comp.* **890**, 161849 (2021).
- [33] V. Petříček, M. Dušek, and L. Palatinus, *Z. Kristallogr. Cryst. Mater.* **229**, 345 (2014).
- [34] A. M. Clogston, *Phys. Rev. Lett.* **9**, 266 (1962).
- [35] A. Inoue, K. Matsuzaki, T. Masumoto, and H. S. Chen, *J. Mater. Sci.* **21**, 1258 (1986).

*email: yuchi@issp.u-tokyo.ac.jp

†email: yokamoto@issp.u-tokyo.ac.jp

Supplementary Note 1. SEM images of a polycrystalline sample of Zr_6RuBi_2 (sample #1).

Enlarged view of Fig. 1(b), which shows SEM image of a polycrystalline sample of Zr_6RuBi_2 (sample #1), and the same view with increased contrast are shown in Supplementary Figs. 1(a) and 1(b), respectively.



Supplementary Figure 1. Enlarged view of Fig. 1(b) in the main text (a) and that with increased contrast (b).

Supplementary Note 2. Details on the powder XRD measurements and crystallographic parameters of Zr_6RuBi_2 (sample #1) and Zr_6FeBi_2 .

Zr_6MTe_2 samples have strong preferred orientation, making them difficult to accurately acquire the intensity of each diffraction peak in the XRD data using the Bragg-Brentano method. Therefore, Debye-Scherrer method was used for Zr_6RuBi_2 (sample #1) and Zr_6FeBi_2 , and then one-dimensional data from all directions were converted to reduce the effect of preferred orientation. In a Debye-Scherrer optical system, Mo $K\alpha$ radiation is generally used, where X-rays can transmit through the sample. On the other hand, since the energy of Mo $K\alpha$ radiation is higher than that of the L-edges of bismuth, the fluorescence X-rays appear as a strong background in the diffraction data. This increases the overall intensity of the diffraction data, resulting in the larger R_{exp} , which is used to evaluate the statistical accuracy of the data. The S values shown in Figs. 1(d) and 1(e) are evaluated using the formula $S = R_{wp}/R_{exp}$, yielding the small S values. In addition, the degree of X-ray absorption strongly correlates with the temperature factor parameters (U_{eq}). In the present cases, strong X-ray absorption causes the loss of quantitativity of the values of U_{eq} , resulting in a small U_{eq} for Fe in Zr_6FeBi_2 .

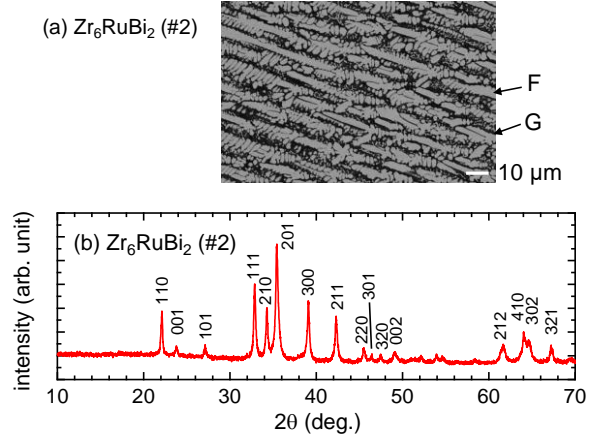
Crystallographic parameters of Zr_6RuBi_2 and Zr_6FeBi_2 determined by the Rietveld analysis on the powder XRD data are listed in Supplementary Table I. The volume ratio of each phase, i.e., that of Zr_6RuBi_2 , ZrRu, and Zr for $M = Ru$ and Zr_6FeBi_2 and Zr for $M = Fe$ in the Rietveld analysis was 80:12:8 and 90:10, respectively.

Supplementary Table I. Crystallographic parameters for Zr_6RuBi_2 and Zr_6FeBi_2 determined by the Rietveld analysis of powder XRD data. The space group is $P-62m$. The lattice parameters are $a = 7.9181(3)$ Å, $c = 3.6847(2)$ Å, and $V = 200.064(17)$ Å³ for Zr_6RuBi_2 and $a = 7.8629(4)$ Å, $c = 3.7174(3)$ Å, and $V = 199.04(2)$ Å³ for Zr_6FeBi_2 .

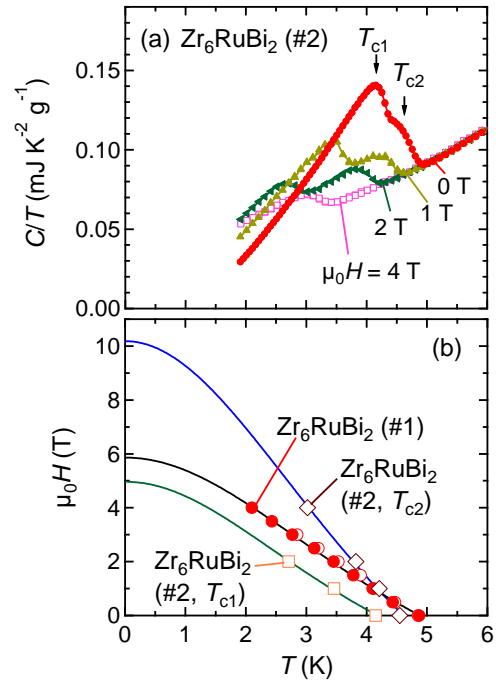
Phase	Atom	x	y	z	g	U_{eq} (Å ²)	
Zr_6RuBi_2	Zr1	3g	0.2455(4)	0	1/2	1	0.0178(13)
	Zr2	3f	0.6053(4)	0	0	1	0.0149(14)
	Ru1	1a	0	0	0	1	0.0152(13)
	Bi1	2d	1/3	2/3	1/2	1	0.0152(6)
Zr_6FeBi_2	Zr1	3g	0.2388(4)	0	1/2	1	0.0293(15)
	Zr2	3f	0.6060(4)	0	0	1	0.0256(16)
	Fe1	1a	0	0	0	1	0.0014(18)
	Bi1	2d	1/3	2/3	1/2	1	0.0219(7)

Supplementary Note 3. Characterization and Physical Properties of Zr_6RuBi_2 (sample #2).

An SEM image and powder XRD pattern of a polycrystalline sample of Zr_6RuBi_2 (sample #2) prepared under different conditions from that for sample #1 are shown in Supplementary Fig. 2. The synthesis procedure is described in the main text. The heat capacity data for Zr_6RuBi_2 (sample #2) are shown in Supplementary Fig. 3.



Supplementary Figure 2. (a) SEM image of Zr_6RuBi_2 (sample #2). (b) Powder diffraction pattern of Zr_6RuBi_2 (sample #2) taken at room temperature using MiniFlex (Cu $K\alpha$).



Supplementary Figure 3. (a) Temperature dependence of heat capacity divided by temperature of a polycrystalline sample of Zr_6RuBi_2 (sample #2) measured at various magnetic fields. (b) Magnetic field versus T_{c1} and T_{c2} for Zr_6RuBi_2 (sample #2). The solid curves show fitting results of T_{c1} and T_{c2} of Zr_6RuBi_2 (sample #2) to the Ginzburg-Landau formula. Data for Zr_6RuBi_2 (sample #1) shown in Fig. 5 are also included here.